

## Design of a room-temperature topological exciton-polariton laser in a ZnO/TiO<sub>2</sub> photonic crystal slab

I. Septembre<sup>1,\*</sup>, C. Leblanc<sup>1</sup>, L. Hermet<sup>1</sup>, H. S. Nguyen<sup>2,3</sup>, X. Letartre<sup>2</sup>, D. D. Solnyshkov<sup>1,3</sup> and G. Malpuech<sup>1</sup>

<sup>1</sup>Université Clermont Auvergne, Clermont Auvergne INP, CNRS, Institut Pascal, F-63000 Clermont-Ferrand, France

<sup>2</sup>Université de Lyon, École Centrale de Lyon, INSA Lyon, Université Claude Bernard Lyon 1, CPE Lyon, CNRS, INL, UMR5270, Écully 69130, France

<sup>3</sup>Institut Universitaire de France (IUF), 75231 Paris, France



(Received 22 December 2022; revised 23 February 2023; accepted 3 April 2023; published 14 April 2023)

We propose theoretically a scheme to get a room-temperature two-dimensional topological exciton-polariton laser with propagating topological lasing modes. The structure uses guided modes in a photonic crystal slab. A ZnO layer provides strong excitonic resonances stable at room temperature. It is capped by a TiO<sub>2</sub> layer pierced by a triangular lattice of air holes. The exciton-polariton modes of the three-dimensional structure are computed by solving numerically Maxwell's equations including the excitonic response. The designed triangular lattice of circular air holes shows a transverse electric band gap. The triangular lattice of air holes is shown to be well described by a staggered honeycomb tight-binding lattice, associated with valley Chern numbers defining the interface states. The interface between two shifted triangular lattices of air holes supports two counterpropagating modes lying in the gap of the bulk modes, analogous to quantum pseudospin Hall interface states. These modes show orthogonal polarizations. They can be selectively excited using polarized excitation and are well protected from backscattering. These modes can benefit from the exciton-polariton gain at room temperature because of their sufficiently large exciton fraction and favorable position in energy. The strong localization of these propagating modes makes them suitable to host topological lasing triggered by a nonresonant pump localized on the interface.

DOI: [10.1103/PhysRevB.107.155304](https://doi.org/10.1103/PhysRevB.107.155304)

### I. INTRODUCTION

Topology is one of the most active fields of research in modern physics. Appearing as a field in the 19th century, it started to grow faster at the end of the 20th century [1,2], first to explain solid-state phenomena [3], and then extended to topological photonics [4–6]. Topological singularities, such as Dirac points [7–10], Weyl points [11–15], or exceptional points [16–19], carry a topological charge describing how the eigenstates evolve critically close to the singularity [20]. The large variety of singularities explains that there are many different topological classes and phases [21–24].

Topological photonics has been initiated by Haldane and Raghu [4,5] and Soljačić's group [25,26]. They proposed to break the time-reversal symmetry (TRS) in photonic crystal slabs (PCSs) in order to mimic the quantum anomalous Hall effect [3] realizing one-way edge modes. This requirement to break TRS first implied working with gyromagnetic materials typically at microwave frequencies. The extension of this regime toward optical frequencies and the key role played by the transverse electric–transverse magnetic (TE-TM) photonic spin-orbit coupling [27] emerged by considering the properties of exciton-polariton modes [28,29]. The key advantage of this broken-TRS phase is that it allows realizing truly topologically protected one-way modes. The disadvantage is

that applying magnetic fields remains inconvenient for future applications, such as integrated photonic circuits.

As a consequence, another class of topological phases, which can be generically labeled the quantum pseudospin Hall effect, became extremely popular in photonics [6]. In analogy with the quantum spin Hall effect [30,31], each pseudospin component of a two-level system is characterized by a topological invariant, which is changing sign through an interface supporting a pseudospin current. These pseudospins can represent the valley degree of freedom in a staggered honeycomb lattice [32], the angular momentum of ring resonators [33], and even light polarization [34] in systems where the permittivity equals the permeability,  $\epsilon = \mu$ , and where the TE-TM splitting is suppressed, or even  $p$  and  $d$  orbitals in shrunken-expanded honeycomb lattices [35,36]. In all these cases, the two pseudospin components must be uncoupled, which is the case if some symmetries are preserved, for example, a crystalline symmetry in the quantum valley Hall effects and shrunken-expanded honeycomb lattices. These modes have interesting properties, such as the possibility to go around sharp corners (of 120°, which preserves the valley), but these interface modes are *a priori* not protected from random local fluctuations of the Hamiltonian (structural disorder), which are necessarily present in real structures. However, it turned out that in staggered and shrunken-expanded honeycomb lattices based on photonic crystal slabs the valley pseudospin is coupled to the circular polarization degree of light [37], providing extra protection against intervalley scattering. A recent work [38] aims at quantifying the topological protection of

\*Corresponding author: ismael.septembre@uca.fr

such interface modes. Recent works have also shown that a staggered honeycomb lattice in a PCS is even not required to get valley-polarized interface states and that using interfaces between triangular lattices of air holes is sufficient [39–41]. In this case, as we show in this paper, the PCS states are still mapped to a tight-binding model with a staggered honeycomb lattice with nonzero valley Chern numbers. This is because the location of the suppressed air hole still hosts an *s*-like state. This state serves as the basis for the upper band. This type of triangular lattice of holes is very advantageous from a technological point of view, since it removes the necessity to create the smallest of the two types of holes of a staggered honeycomb lattice PCS.

One of the most emblematic devices born in the field of topological photonics is the topological laser, where lasing occur on topological edge or interface states. It took some time for the community to propose this concept, probably because topological photonics was initially developed in a wavelength range for which gain is essentially absent. A topological laser was proposed based on a one-dimensional (1D) Su-Schrieffer-Heeger (SSH) chain of zero-dimensional (0D) exciton-polariton modes [42], which is a type of system where lasing occurs quite naturally [43,44]. It was then proposed in purely photonic 1D lattices [45], where the term “topological lasing” was introduced. It was experimentally realized soon after at low temperature in a polaritonic system [46–48] using etched microcavities. Slightly later, two-dimensional (2D) topological lasers hosting propagating edge or interface modes were proposed [49] and realized either in broken-TRS phases (quantum anomalous Hall effect) [50] or in a quantum pseudospin Hall effect setting [51]. Since then, the field considerably expanded. One can cite the realization of electrically pumped 2D topological lasers first at low temperature using valley edge modes [52], and then at room temperature with ring resonator lattices [53]. In strongly coupled polaritonic systems, a 1D room-temperature topological polariton laser [47] showing high coherence [48] has been demonstrated in organic-based systems. 2D topological lasers based on coupled-cavity lattices under magnetic field were proposed [54], but in a scheme typically limited to low temperatures. The quantum pseudospin Hall effect has been implemented at room temperature using transition metal dichalcogenide monolayers placed on PCSs [55], but lasing has not yet been demonstrated. Historically, the achievement of room-temperature polariton lasing has relied on using large-band-gap semiconductors, ZnO and GaN, first in microcavities [56–59], then using guided polariton modes [60–62], which allows long propagation distances ( $\sim 100 \mu\text{m}$ ).

In this work, we propose a feasible design of a 2D room-temperature topological polariton laser with propagative interface states. The waveguide structure is composed of a ZnMgO cladding, of a ZnO layer providing strong and stable excitonic resonances, and of a TiO<sub>2</sub> layer with a high refractive index. The latter is etched with a triangular lattice of circular air holes. We solve numerically Maxwell’s equations by finite element method for a three-dimensional (3D) structure periodic in the  $(x, y)$  plane and find the dispersion of 3D polaritonic modes, the excitonic resonance being taken into account in the permittivity. We find a gap in the dispersion of TE modes of 50 meV width, whose energy can be set up to

3.25 eV with an exciton fraction of gap edge modes around 0.2, which are favorable parameters to get room-temperature polariton lasing in ZnO-based materials [59,60]. We then model a 3D structure hosting topological interface states by creating an interface between two triangular lattices with the same parameters, without resorting to a staggered honeycomb lattice. Numerical constraints do not allow finding directly the polaritonic modes in such a structure, so we compute the bare photonic modes and describe the coupling between those modes and the ZnO excitonic resonances through an effective Hamiltonian. We show that by exciting the interface with a well-defined circular polarization, the propagation occurs only at the interface and in a unique direction with a very good selectivity. We finally discuss the possibility to trigger polariton lasing specifically at the interface states using a focused nonresonant optical pumping, because its overlap with the interface modes can be made considerably larger than with bulk states. The scheme we propose could be used for developments in integrated photonics and/or polaritonics, that is, on-chip integration of room-temperature topological polariton lasers.

## II. TOPOLOGICAL INTERFACE IN A TRIANGULAR LATTICE

In this section, we demonstrate that the interface between two triangular lattices (which have the same geometric parameters) can host propagative interface states in the gap of the bulk bands.

We begin by considering a *honeycomb* lattice of circular holes. The TE band structure with the electric field of the eigenstates localized inside the air holes exhibits conical intersections (Dirac points) at the corners of the Brillouin zone ( $K$  and  $K'$ ) [63]. In a tight-binding description of such a lattice, the two Dirac points are characterized by opposite winding  $\pm 1$  of the sublattice pseudospin. The staggering of the lattice makes sites A and B different. It opens a gap at the two  $K$  and  $K'$  points, also called valleys. The Berry curvature of bands is opposite in the two valleys, so a valley Chern number can be defined. It has opposite signs at  $K$  and  $K'$ . Making an interface between two lattices with opposite staggering and inverted valley Chern numbers realizes the so-called quantum valley Hall effect, where the direction of propagation of interface modes is associated with a given valley.

Figures 1(a) and 1(b) show the TiO<sub>2</sub> 2D photonic crystal (PC) we simulate [Fig. 1(a)], together with its dispersion [Fig. 1(b)] obtained by 2D simulations using COMSOL MULTIPHYSICS. In this section, we restrict our simulations to 2D structures for simplicity, because we focus on the effects of different kinds of patterning which are already visible in two dimensions. The software solves the Helmholtz equation:

$$\nabla \times (\nabla \times \mathbf{E}(\mathbf{r})) = k^2 \epsilon_r(\mathbf{r}) \mathbf{E}(\mathbf{r}), \quad (1)$$

where  $\mathbf{E}(\mathbf{r})$  is the electric field profile,  $\epsilon_r(\mathbf{r})$  the permittivity tensor, and  $k$  the wave vector. It finds the spatial profiles and the energies of the eigenmodes. The structure we simulated is schematically shown in Fig. 1(a). It is a ribbon in the  $y$  direction and an infinite structure in the  $x$  direction using Floquet periodicity. The interface is a line in the  $x$  direction. We took a ribbon of 16 periods in the  $y$  direction both for

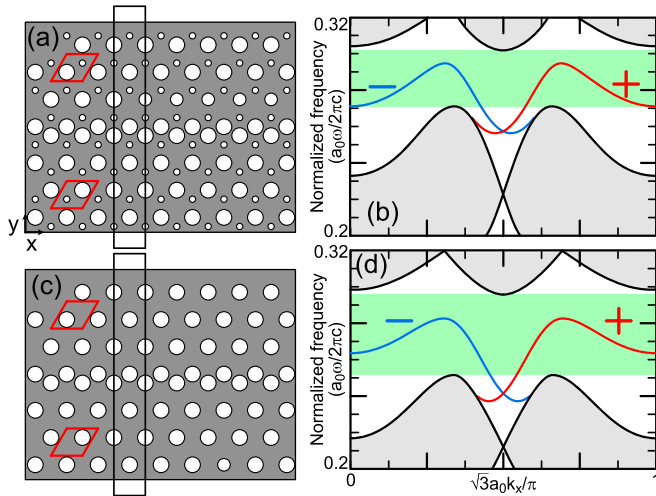


FIG. 1. 2D simulations demonstrating the presence of topological interface states even with a triangular lattice. [(a), (c)] PC of circular air holes in a dielectric matrix and topological interface using (a) a staggered honeycomb and (c) a triangular lattice of air holes. The unit cell is emphasized in red, showing the difference between the upper and lower PCs. The triangular lattice is obtained by continuously reducing and ultimately removing the small hole of the staggered honeycomb lattice. A ribbon of  $a_0$  width along the  $x$  direction and several periods in the  $y$  direction, as used in the simulations to emulate an infinite system in the  $x$  direction, is surrounded by black lines. [(b), (d)] Band structures with interface states (blue and red lines excited by a  $\sigma_{\pm}$ -polarized pump) in the gap (green area) of the structures with topological interfaces of (b) staggered honeycomb and (d) triangular lattices. The bulk modes (grey areas) are delimited by black thick lines. Note that interface states exist in both cases, whereas the gap is much larger in the triangular PC.

the PC above and below the interface. We can see that the upper PC has a staggering opposite to the one of the lower PC, as emphasized by the unit cells in red (the lattice constant is noted  $a_0$ ). The dispersion of the TE modes of the structure is plotted in Fig. 1(b) where the energy is calculated in reduced coordinates, the radii of the small and big holes being  $R_- = 0.1a_0$  and  $R_+ = 0.25a_0$ , respectively.

We see that there is an energy range (green area) where no bulk states (grey areas surrounded by black lines) are present. This area is the band gap. To have this gap close to the exciton energy in ZnO and GaN (around 3.2–3.4 eV) one needs to take  $a_0 \sim 100$  nm corresponding to a small hole radius around  $R_- \approx 15$  nm, which is extremely challenging from the technological point of view. Inside the gap, there are two interface states (red and blue lines) with a nonzero group velocity. Because those states are in the gap of both the upper and lower PCs, they cannot scatter into the bulk states, so they propagate only at the interface with the direction of propagation associated with a valley.

The size of the gap is crucial in determining how well the interface states will be isolated from bulk states. It is determined by the radii of the two holes: if they are equal, the gap is null (there is a Dirac point), and the gap increases as they become more and more different [63,64]. The limit  $R_- = 0$  is a triangular lattice of circular holes, as represented in Fig. 1(c). It presents a particularity: a straightforward

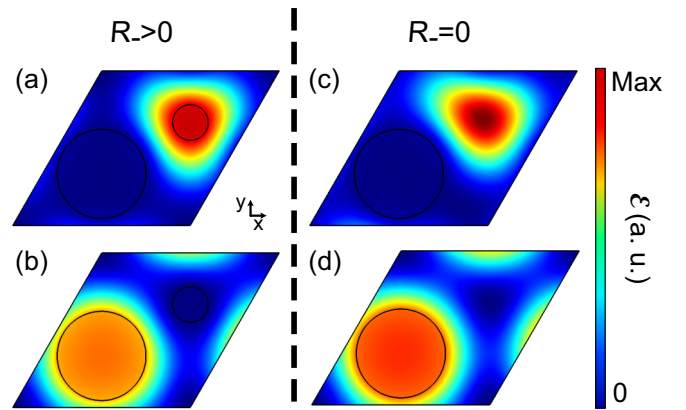


FIG. 2. 2D simulations demonstrating the equivalence between a staggered honeycomb lattice of air holes and a triangular lattice of air holes. [(a), (b)] Electromagnetic energy density in a unit cell for  $R_- = 0.1a_0$  and  $R_+ = 0.25a_0$  at the  $K$  point. This corresponds to a staggered honeycomb lattice of air holes. [(c), (d)] Electromagnetic energy density in a unit cell for  $R_- = 0$  and  $R_+ = 0.25a_0$  at the  $K$  point. This corresponds to a triangular lattice of air holes. (a) and (c) are the higher energy states while (b) and (d) are the lower energy states. Note the continuous deformation from (a) to (c).

calculation for a tight-binding triangular lattice gives zero Berry curvature, but there is no topological transition separating this limit from the phase with nontrivial valleys at  $R_- \neq 0$ , because the band is globally trivial. The symmetry indicators, calculated from the wavefunction at the high-symmetry points of the reciprocal space and allowing to determine the topology without integrating the Berry curvature over the whole Brillouin zone [65], also do not change [39,66,67]. We compute the dispersion in this case (with the same  $R_+$ ) and plot it in Fig. 1(d), and find that the interface states still exist in the gap, and the gap is much larger. This is in agreement with recent numerical and experimental studies [39–41,67]. Moreover, we can see that this situation is advantageous because it makes a bigger gap, which leads to an energy range where a mode of a given circular polarization propagates in only one direction. This can be found as well in a staggered honeycomb of air holes with different parameters [64], but the region where the states are unidirectional is always larger for a triangular lattice of air holes compared to the same lattice containing a small hole.

In a PC, staggered honeycomb and triangular lattices are topologically equivalent and going from one to another represents a continuous deformation. This is demonstrated by Fig. 2 showing the profile (electromagnetic energy density  $\mathcal{E}$ ) of the two bulk modes at the  $K$  point in a unit cell of a PC with a staggered honeycomb lattice of air holes [Figs. 2(a) and 2(b)] and with a triangular lattice of air holes [Figs. 2(c) and 2(d)]. We see that the profile of the lower energy state [Figs. 2(b) and 2(d)] does not change much when the small air hole disappears, as expected, because it is anyway confined mostly in the big air hole. The second mode (of higher energy) in both cases is shown in Figs. 2(a) and 2(c). It is very similar as well, and we see that the suppression of the small air hole does not drastically change the profile of the mode. We can conclude that in both cases, the appropriate tight-binding description

for these modes is provided by a staggered honeycomb lattice. When the two air holes are of the same size, the states confined in both holes have the same energy, and the dispersion shows a Dirac point. When we reduce one air hole, the energy of the two modes becomes different and a gap opens at the Dirac point. The energy difference between the two modes increases when one hole is reduced, and it could be increased even beyond the value obtained for a vanishing hole, if a higher-index material cylinder is inserted at the hole's location.

In the following, we capitalize on this behavior that facilitates the fabrication of structures and study a 3D polaritonic structure with two PCSs of simple triangular lattices of circular holes.

### III. PHOTONIC CRYSTAL SLAB WITH EXCITON-POLARITONS IN ZnO

The photonic crystal slab structure we consider is schematically depicted in Fig. 3(a). It consists of a two-layer waveguide isolated from the substrate by a cladding layer (ZnMgO). The waveguide is made of patterned TiO<sub>2</sub> PCS (thickness  $h_0$ ) and a bulk ZnO layer (thickness  $h_{\text{ZnO}}$ ). The PCS consists of a triangular lattice of circular holes. The lattice constant is  $a_0$  and the diameter is  $2R$ . This part of the waveguide provides the topological properties of the guided mode, whereas the ZnO part provides the strong coupling with an excitonic resonance, giving rise to exciton-polaritons. The structure we consider directly comes out of the specifications explained hereafter. We want to build a structure capable of robust lasing behavior at room temperature so that it could be used in integrated photonics to pump photonic circuits. The lasing mechanism we want to use comes from the bosonic nonlinearity of exciton-polaritons, giving rise to polariton lasing in the guided configuration [60]. One, therefore, needs to fabricate a photonic crystal slab structure on a substrate, and not free standing, to provide efficient heat dissipation. Moreover, the room-temperature specification requires the use of wide-band-gap semiconductors, and the robustness restrains the choice essentially to GaN and ZnO. We have considered both and have finally chosen to focus on ZnO because of the following reasons.

Nowadays, ZnO can be grown on ZnMgO (itself grown on a ZnO or sapphire substrate) with a very good quality [68]. The ZnMgO layer serves as an optical cladding for the ZnO core, isolating it from the substrate, and as a buffer improving the growth quality. The best quality is obtained with  $m$ -plane ZnO [68]. However, the refractive indices of ZnO and ZnMgO are too close to each other, which prevents one from making a PCS by patterning directly the ZnO, because patterning makes its effective index smaller than that of ZnMgO, which suppresses the vertical confinement. Thus, we suggest using an extra layer with an effective index higher than that of ZnO for patterning. The TiO<sub>2</sub> is a particularly good candidate because of well-developed deposition and etching techniques.

After deposition, the PCS is formed by etching only the TiO<sub>2</sub> layer. Close to the exciton resonance of ZnO ( $E_X \approx 3380$  meV), the refractive index of TiO<sub>2</sub> is high ( $n_{\text{TiO}_2} \approx 3$ ) and the losses are sufficiently low ( $k_{\text{TiO}_2} \approx 10^{-4}$ ) [69]. Etching it can give a slab with an effective refractive index of about 2.2, close to the one of ZnO at these energies [68]. We

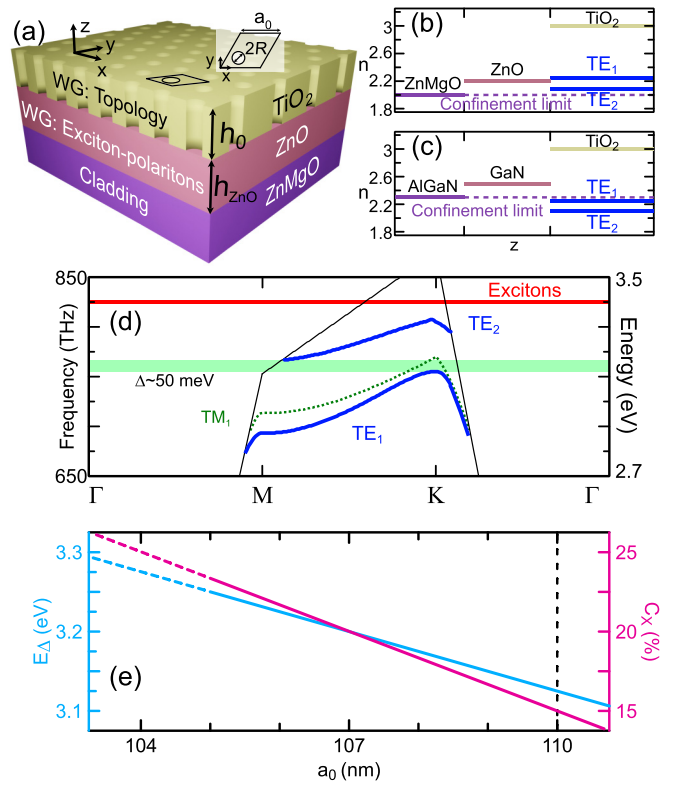


FIG. 3. (a) Scheme of the PCS structure studied. A two-layer waveguide (TiO<sub>2</sub> in yellow and ZnO in pink) is separated from the substrate by a cladding layer (ZnMgO in purple). Only the TiO<sub>2</sub> layer is etched with a triangular lattice of circular holes. The thicknesses of the TiO<sub>2</sub> layer,  $h_0$ , and ZnO layer,  $h_{\text{ZnO}}$ , are indicated. The 3D unit cell is shown in black and a 2D cut of it in the TiO<sub>2</sub> layer is shown in the inset with the geometric parameters of the lattice,  $R$  and  $a_0$ . [(c), (d)] Refractive indices of the different layers in the  $z$  direction for a structure using (b) ZnO and (c) GaN. The effective indices of the TE<sub>1,2</sub> modes are indicated in blue. (d) Dispersion of the three modes below the exciton energy. There are two quasi-TE modes (blue solid lines) and one quasi-TM mode (green dashed line). The TE gap is emphasized by the light green area. Black lines represent the light cones; only modes below them are guided. Exciton energies are close and represented as a unique thick red line. (e) Energy of the center of the gap,  $E_\Delta$ , and exciton fraction  $C_X$  with respect to the period of the lattice,  $a_0$ . The dispersions plotted in this work correspond to  $a_0 = 110$  nm, represented as a vertical dashed line.

represent schematically the refractive indices of the different layers in Fig. 3(b), showing that the etched TiO<sub>2</sub> layer provides light confinement for the two first TE modes TE<sub>1,2</sub>. A similar analysis is displayed in Fig. 3(c) for an AlGaIn/GaN/TiO<sub>2</sub> structure. It shows that TE modes are not confined in this structure, because of the excessive value of the AlGaIn refractive index (for  $\sim 20\%$  of Al). A GaN-based structure would require a dielectric layer with a larger refractive index and small losses around the GaN exciton energy (around 3.5 eV).

In the simulations, we use frequency-dependent anisotropic permittivities for ZnO and ZnMgO layers [69] and isotropic for TiO<sub>2</sub>. For ZnO, the  $m$ -plane growth brings in-plane anisotropy of both the background permittivity and the exciton resonances. Thus, in the  $(x, y, z)$  basis,

we have

$$\epsilon_{\text{Zn(Mg)O}} = \begin{pmatrix} \epsilon_{\text{Zn(Mg)O}}^{\parallel}(\omega) & 0 & 0 \\ 0 & \epsilon_{\text{Zn(Mg)O}}^{\perp}(\omega) & 0 \\ 0 & 0 & \epsilon_{\text{Zn(Mg)O}}^{\perp}(\omega) \end{pmatrix}. \quad (2)$$

The ZnO exciton response is taken into account in the permittivity [70]:

$$\epsilon_{\text{ZnO}}(\omega) = \epsilon_{\infty} + \sum_{i=A,B,C} \frac{f_i}{\omega_i^2 - \omega^2}, \quad (3)$$

where  $A$ ,  $B$ , and  $C$  are the excitons of ZnO,  $f_i$  their respective oscillator strengths, and  $\omega_i$  their respective resonance frequencies. The nonradiative exciton lifetime can be added as an imaginary part. The permittivity of  $\text{Zn}_{1-x}\text{Mg}_x\text{O}$  is taken from Ref. [71] for  $x \approx 0.2$ , while the one of ZnO is extracted from Ref. [68]. For ZnO, the exciton resonances are located approximately at 3375 meV ( $A$ ), 3380 meV ( $B$ ), and 3410 meV ( $C$ ) at room temperature, while the oscillator strengths are approximately  $f_A = 1.5 \times 10^5 \text{ meV}^2$ ,  $f_B = 2.5 \times 10^5 \text{ meV}^2$ , and  $f_C = f_A + f_B$ .

Because we now consider a 3D structure, TE and TM modes are ill defined, but we can still distinguish between quasi-TE and quasi-TM modes, the modes that are the 3D extensions of TE and TM modes, respectively. Numerically, COMSOL finds all photonic modes (quasi-TE and quasi-TM), and we only keep the quasi-TE modes by comparing the values of the electric and magnetic fields along the  $z$  direction. For TE modes,  $E_z = 0$ , and for TM modes,  $H_z = 0$ . So, the 3D modes with a large ratio  $|E_z|/|H_z|$  are the quasi-TM modes, whereas those where the ratio is small are the quasi-TE modes (the ones that we keep).

The dispersion of the quasi-TE polariton modes is plotted in Fig. 3(d) for the path  $\Gamma$ - $M$ - $K$ - $\Gamma$  in the reciprocal space, which follows high-symmetry points of the lattice. Despite the broken symmetry along the  $z$  direction and the presence of excitons, the dispersion is quite typical for this kind of PCS, although flattened. Because we work with guided modes, we are interested in the modes that lie below the light cone. Moreover, we notice a gap between the two quasi-TE bands. This gap is centered around 3125 meV and of amplitude  $\Delta \approx 50 \text{ meV}$ . We calculated the exciton fraction  $f_X$  of the modes near the gap edges by comparing the group velocity with excitons,  $v_X = \partial E_{\text{ep}}/\partial k$ , and without them,  $v_0 = \partial E_{\text{p}}/\partial k$ , where  $E_{\text{ep}}$  is the energy of the lower polariton branch. In the end, we find  $f_X = 11 \pm 2\%$  for the interface states, which is sufficiently large to observe polariton lasing [59,60].

The size of the gap reaches such a value for the set of parameters  $h_{\text{ZnO}} = 50 \text{ nm}$ ,  $h_0 = 130 \text{ nm}$ ,  $a_0 = 110 \text{ nm}$ , and  $2R = a_0/2 = 55 \text{ nm}$ , according to our optimization study. Those dimensions, although challenging to obtain, must be achievable in state-of-the-art realizations, especially because we use a circular geometry for holes. The main challenge is to etch holes of such small diameter with a depth of more than 100 nm. It could happen that the holes are not completely etched, meaning that they have the correct diameter but they do not reach the ZnO layer. We performed additional simulations proving that a deviation of the order of a few nanometers

of the depth of etching does not affect the results we present below.

However, we noticed that under-etching (the situation that is more probable experimentally) is less deleterious than over-etching (which is anyway less probable experimentally). In the following, we consider that the  $\text{TiO}_2$  slab is completely etched, and the ZnO layer remains intact.

There are no propagative quasi-TE states at the energies lying inside the gap. However, we show that there is still a quasi-TM mode that is inside the quasi-TE gap [in Fig. 3(d), the dashed green line is the quasi-TM mode which is inside the green area, the quasi-TE gap]. It has a very small overlap with the quasi-TE modes, so it will be disregarded as in the other works [36,37,64]. A complete band gap for both quasi-TE and quasi-TM modes requires a very strong anisotropy of the refractive indices between in-plane and out-of-plane components [63], and the anisotropy that we have in ZnO, despite being not negligible, is still too weak. However, we note that, due to the exciton resonance, the second TM mode (the mode  $\text{TM}_2$ ) is not present below the exciton resonance. This means that there is an effective TM gap starting from the  $\text{TM}_1$  mode up to the next mode, which is above the exciton. This is an interesting feature that we think may be used to create a PCS with a full quasi-TE and quasi-TM band gap.

Figure 3(e) shows the energy of the center of the gap,  $E_{\Delta}$ , with respect to the lattice constant  $a_0$  for the same structure. The size of the hole is varied accordingly, in order to keep the filling factor of the  $\text{TiO}_2$  layer constant. The closer to the exciton we are, the higher the energy and the exciton fraction. When the energies are too high ( $E_{\Delta} > 3.25 \text{ eV}$ ), the modes cross the light cone, the confinement is lost, and they penetrate into the cladding (the dashed lines continuing the solid lines). One can engineer the position of the center of the gap and the exciton fraction to get a polariton laser, as we will discuss later. The vertical dashed line indicates a period of  $a_0 = 110 \text{ nm}$ , which corresponds to the situation considered in Fig. 3(d). This leads to an energy of the middle of the gap of  $E_{\Delta} \approx 3125 \text{ meV}$  and an exciton fraction of approximately  $C_X \approx 15\%$ .

#### IV. INTERFACE STATES IN THE 3D PCS STRUCTURE

We now consider the structure discussed before, but the top layer is now composed of two triangular lattices of circular holes shifted with respect to each other, forming an interface. A scheme of the top layer is shown in Fig. 1(c) and the full 3D structure is represented in Fig. 4(a). Here, the symmetry in the  $z$  direction is broken and one needs to check if the results of the 2D case (Fig. 1) are still valid. The structure we consider is a triangular lattice of circular air holes, infinite in the  $x$  direction and 24-period large in the  $y$  direction. The upper half of the PCS is translated in the  $y$  direction by  $\delta y = -a_0\sqrt{3}/6$ , which creates an interface between two triangular lattices of air holes. We use the same parameters as before, that is,  $a_0 = 110 \text{ nm}$  and  $2R = 55 \text{ nm}$ .

The knowledge of the permittivity of each material should be sufficient to find the dispersion of the structure, as we did for Fig 3(d). However, the strong variation of the permittivity

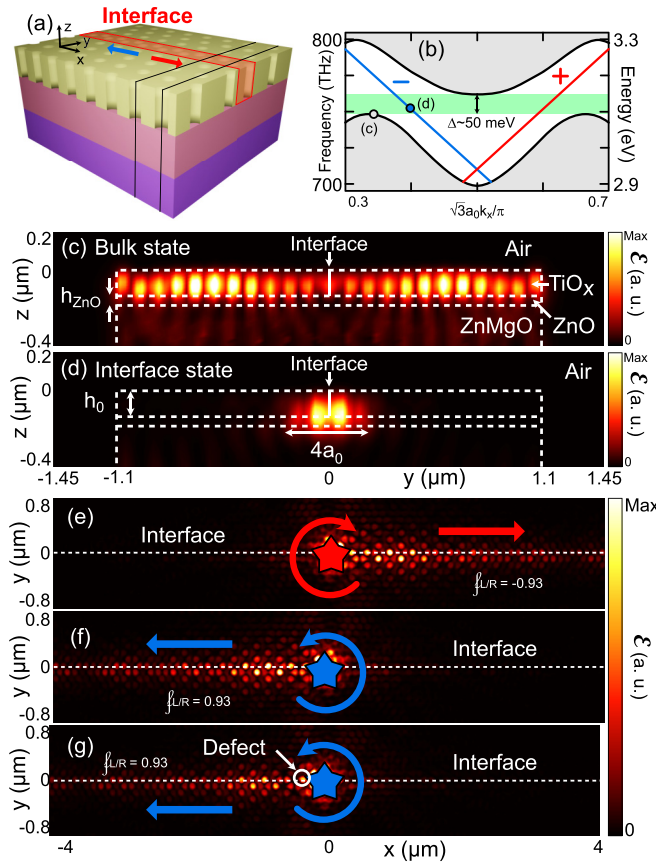


FIG. 4. (a) Sketch of the 3D PCS structure hosting topological interface states. The slabs are the same as previously ( $\text{TiO}_2$  in yellow, ZnO in pink, and ZnMgO in purple), but the top layer now contains an interface between two PCSs of triangular lattices of circular holes (emphasized in red), where interface states can propagate in the left (blue) or right (red) direction. The black lines mark the 3D ribbon used in the simulations. (b) Polaritonic band structure calculated for a finite ribbon in the  $y$  direction and infinite structure in the  $x$  direction, including the interface. Note the interface states that can propagate in the gap formed by the bulk modes. An excitation with circular right (left) polarization leads to propagation in the right (left) direction (red and blue lines). [(c), (d)] Electromagnetic energy density profiles of (c) the bulk state and (d) the interface state calculated from COMSOL. The corresponding states of these profiles in the dispersion (b) are indicated by the grey (blue) point for the bulk (interface) state. [(e), (f)] Profiles of the interface states calculated by FDTD under (e) a circular right-polarized excitation and (f) a circular left-polarized excitation located below the interface. Note that the propagation occurs mainly in the right or left direction (dashed white line). (g) Same as (f), but with a defect at the interface. Note the very good similarity between (g) and (f).

close to the exciton resonance prevents COMSOL from finding the eigenstates properly [72]. To circumvent this problem, we look for the dispersion of purely photonic modes  $E_p(k)$  (neglecting the exciton resonance), and we postprocess them to include properly the coupling to an effective excitonic resonance. For that purpose, we use the matrix describing the strong coupling of excitons and photons [44,70,73,74],

$$M_{SC} = \begin{pmatrix} E_X & \rho \hbar \Omega_R \\ \rho \hbar \Omega_R & E_p(k) \end{pmatrix}, \quad (4)$$

where  $2\hbar\Omega_R = 125$  meV is the estimated Rabi splitting for the thicknesses of ZnO that we deal with [75–77],  $E_X = 3380$  meV is the energy of the exciton (we consider only one exciton resonance of the polarization corresponding to the TE photonic bands), and  $\rho$  is the fraction of the mode confined in the ZnO layer. It is really important to take it into account because the waveguide we consider contains two layers, and thus an important part of the mode is not confined in ZnO, but rather in the PCS, which does not contain any exciton. We simulate this structure in COMSOL and find the dispersion  $E_p(k)$  of photonic modes and their spatial distribution to extract  $\rho$ . The lower energy band (mode  $\text{TE}_1$ ) is less confined in ZnO ( $\rho \sim 10\%$ ) than the upper energy band (mode  $\text{TE}_2$ ) for which the confinement in ZnO is approximately  $\rho \sim 20\%$ , which is also the case for the interface modes. We neglect the wave-vector dependence of the exciton energy.

As a next step, we diagonalize matrix (4) and find the polaritonic dispersion:

$$E_{LP} = \frac{E_X + E_p(k)}{2} - \sqrt{(\rho \hbar \Omega_R)^2 + \left(\frac{E_X - E_p(k)}{2}\right)^2}. \quad (5)$$

The corresponding band structure is plotted in Fig. 4(c). It is consistent with the band structure found in Fig. 3(d), but the structure is here infinite only in the  $x$  direction. We still find a band gap for the bulk states at the same energy and of the same amplitude  $\Delta \approx 50$  meV, but now there are two modes in the gap of the bulk states, which are localized at the interface between the two triangular lattices of air holes. The two states are counterpropagating, one going in the  $+x$  direction and the other going in the  $-x$  direction, as expected. The group velocity of the interface states is  $v_g = 25$   $\mu\text{m}/\text{ps}$ , which is consistent with the existing literature [78].

We note that Eq. (4) is written for a single photon polarization (the one of the bulk modes), which couples to a single exciton. The interface modes are circularly polarized, so they also couple to the other exciton. This aspect is neglected in our calculation, because the anisotropy of the exciton response at the frequencies of the interface modes (up to the highest exciton fraction considered) is less than 7%. It is just 1% at the frequency of the interface modes shown in the paper. We consider that such error is negligible with respect to the other uncertainties (including the experimentally measured exciton response itself).

In Figs. 4(c) and 4(d), we show the spatial profile (obtained from the electromagnetic energy density  $\mathcal{E}$ ) in the  $(y, z)$  plane of the mode corresponding to the grey and blue points in Fig. 4(b), respectively. We can see that the state corresponding to the grey point is not localized at the interface, but rather spread in the bulk of the PCS, while the state corresponding to the blue point is strongly localized at the interface, with a very narrow profile of only a few periods in the  $y$  direction. We conclude that the blue line indeed corresponds to interface states, while the bulk states are in the grey regions, as expected.

So far, the interface modes are just two states of opposite wave vectors propagating in opposite directions. One could think that they could elastically scatter (by disorder) from one to another, which would give rise to Anderson-localized states. However, the interface state propagating to the right

[+ states in Fig. 4(b)] is circularly polarized  $\sigma^+$  on one side of the interface and  $\sigma^-$  on the other side. The counter-propagating mode [−states in Fig. 4(b)] shows the opposite polarization pattern. These features can be found both from a tight-binding description of a staggered honeycomb lattice with TE-TM splitting and by examining the electric field pattern of modes numerically computed by COMSOL. These two counterpropagating states are orthogonal from a polarization point of view which prevents scattering from one to another by elastic scattering on the structural disorder. This protection from backscattering occurs for the vectorial electromagnetic field (photons), but does not *a priori* hold for the electronic quantum valley Hall effect.

Next, we further illustrate this crucial property by simulating the propagation of wave packets on the interface. This can be numerically simulated by using the finite difference time-domain (FDTD) method. Time-dependent simulations are realized using the software LUMERICAL. We used it to solve time-dependent Maxwell equations [including excitonic contributions in the permittivity given by Eq. (2)] in this structure and probe the existence of interface states. By choosing the excitation position and polarization, it is possible to excite unidirectional interface states at a topological interface between two PCSs [79]. We use this method and pump the interface with a circular left or circular right polarized electric dipole with frequency  $f \approx 755$  THz, corresponding approximately to the center of the gap [see Fig. 4(b)]. We then observe the propagation of the interface state for a few picoseconds and a few micrometers, as expected from the dispersion. In Figs. 4(e) and 4(f), we plot the electromagnetic energy density. The image is plotted in the middle of the  $\text{TiO}_2$  slab,  $\sim 100$  fs after the beginning of the simulation. The excitation pulse duration is chosen to be sufficiently long ( $\delta\tau \sim 1$  ps) to be narrow in frequency ( $\delta f \sim 1$  THz). We can see from the image that the propagation is mainly at the interface and that the signal propagates to the right (left) of the injection point if the excitation is polarized circular right in Fig. 4(e) [left in Fig. 4(f)], as expected [79]. Indeed, we pump below the interface for both images, so that the direction of propagation of the topological interface states is given only by the polarization of the excitation. Note that exciting above the interface leads to inverted results, meaning that exciting circularly right (left) implies propagation to the left (right), because of the preserved chiral symmetry.

We calculate the directional selectivity (left-to-right) ratio,

$$f_{L/R} = \frac{P_L - P_R}{P_L + P_R}, \quad (6)$$

where  $P_{L/R}$  is the magnitude of the Poynting vector far from the injection ( $\sim 4 \mu\text{m}$  away) integrated over a narrow 2D zone of few periods in both  $x$  and  $y$  directions and normalized. In the end, we find  $f_{L/R} = -0.93 \pm 0.04$  for an excitation with circular right polarization and  $f_{L/R} = 0.93 \pm 0.04$  for an excitation with circular left polarization, which confirms a very high selectivity.

Moreover, we perform an additional simulation to verify that defects at the interface do not prevent topological interface states to propagate. We reproduce the simulation of Fig. 4(f), but we double the radius of one hole at the interface, on the path of the propagating topological interface state. The

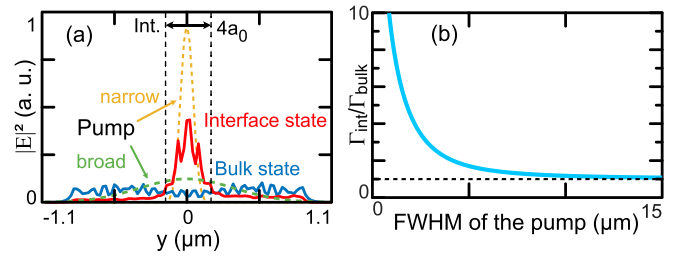


FIG. 5. (a) Electric field profile (square amplitude) of the pump (dashed lines) and states (solid lines) in the  $y$  direction. The norm of the electric field of the states is integrated along the  $x$  and  $z$  directions (and restricted to the ZnO) to give the profile. A broad pump has a good overlap with the interface states while the overlap is smaller for a narrow pump. (b) Ratio between the overlap of the pump profile with the interface  $\Gamma_{\text{int}}$  and bulk  $\Gamma_{\text{bulk}}$  states with respect to the size of the Gaussian pump, here its full width at half maximum (FWHM). A ratio of 1 is indicated by the dashed line.

profile of the mode is shown in Fig. 4(g), where we can see that, despite the defect indicated with a white circle, the profile of the mode is very similar. We calculate in this case the directional selectivity ratio and find  $f_{L/R} = 0.90 \pm 0.03$ , which is a bit lower than the one found without defect, but still very close to one, as expected. We estimate that the backscattering on the defect is about 3%, which is very low. This can be attributed to the topological nature of the states. However, it is not completely zero, because scattering to the opposite polarization is still possible although minimized by the polarization properties of the modes.

## V. TOPOLOGICAL POLARITON LASING

By itself, the presence of interface states does not ensure that there can be lasing from them. There is first a need for gain, which can be electron-hole gain in a standard laser or polaritonic gain in a polariton laser. Room-temperature polariton lasing in ZnO cavities [59] and waveguides [60] has already been reported. In these references, lasing was achieved around 3.2–3.25 eV with exciton fractions  $C_X$  of the order of 20%. In the previous sections, we considered a structure showing a gap at approximately 3.1–3.15 eV. Figure 3(e) shows the energy of the center of the gap,  $E_\Delta$ , versus the lattice period  $a_0$  for the structure without interface. We find that the upper side of the gap remains below the light cone up to 3.25 eV for the energy of the gap center. We conclude that a topological gap around 3.2 eV is feasible ( $a_0 = 107$  nm), which allows keeping the interface modes below the light cone, but it is the maximum value that can be achieved. The corresponding interface state shows an exciton fraction around 0.2, slightly larger than modes having the same energy in bulk cavities, because the overlap between the electric field and excitons is a little bit better in guided geometry.

The second condition to get topological lasing is that mode competition should favor the topological interface states instead of bulk states. The most efficient approach is to focus the nonresonant pump laser on the topological state (on the interface), as proposed in Ref. [42] and done in Ref. [46]. Figure 5(a) shows the spatial distribution along  $y$  of the interface mode at 3.2 eV and of a bulk state. They

exhibit a small overlap. The thin dashed lines represent two Gaussian excitations (narrow and broad). The ratio between the pump-to-interface  $\Gamma_{\text{int}}$  and the pump-to-bulk  $\Gamma_{\text{pump}}$  overlap versus the full width at half maximum (FWHM) of the Gaussian is shown in Fig. 5(b). This ratio can be made arbitrarily large by considering a large sample, which increases the size of the bulk only. The qualitative conclusion is that a typical micrometer-sized pump laser excites the interface modes more than the bulk modes. For a pump smaller than  $\sim 4 \mu\text{m}$ , the overlap with the interface states is twice larger than with the bulk states. The overlap between the pump and the interface states is always better than with bulk states [the ratio  $\Gamma_{\text{int}}/\Gamma_{\text{pump}}$  is always larger than 1; see the dashed line in Fig. 5(b)], which favors lasing specifically on the interface states rather than on bulk states.

Another requirement is that lasing occurs on the interface states lying in the gap, rather than interface states outside the gap that are resonant with bulk modes. In practice, interface modes out of the gap are expected to suffer losses due to their coupling to the bulk modes by elastic scattering on the disorder, which is extremely significant in this frequency range so that the in-gap interface states are expected to be strongly favored. On the other hand, both interface modes propagating in opposite directions are expected to be excited by the nonresonant pump, as was the case in previous papers reporting topological lasers based on the quantum pseudospin Hall effect [51]. This can be overcome by using a circularly polarized nonresonant pump spatially shifted with respect to the interface, similarly to what is done in this work. Such

pumping should favor one of the two interface modes leading to directional lasing, provided the generated exciton reservoir does not lose completely its polarization.

## VI. CONCLUSION

To conclude, we propose a realistic design for a room-temperature 2D topological polariton laser. We model the full 3D structure of a photonic crystal slab including a ZnMgO cladding, an active ZnO layer, and a patterned TiO<sub>2</sub> layer. The full structure demonstrates a quasi-TE gap for bulk modes and topological interface states in this gap, whose energy and exciton fraction are optimal to get room-temperature polariton lasing. We find that the topological interface states have an excellent one-way character upon appropriate excitation, because they are protected from backscattering by their polarization.

## ACKNOWLEDGMENTS

We thank N. Gippius, J. Zúñiga-Pérez, S. Bouchoule, E. Cambril, T. Guillet, and J.-Y. Duboz for useful discussions. This research was supported by the ANR Labex GaNext (ANR-11-LABX-0014), the ANR program “Investissements d’Avenir” through the IDEX-ISITE initiative 16-IDEX-0001 (CAP 20-25), the ANR project “NEWAVE” (ANR-21-CE24-0019), and the European Union’s Horizon 2020 program, through a FET Open research and innovation action under Grant Agreement No. 964770 (TopoLight).

- 
- [1] D. J. Thouless, M. Kohmoto, M. P. Nightingale, and M. den Nijs, *Phys. Rev. Lett.* **49**, 405 (1982).
- [2] M. V. Berry, *Proc. R. Soc. London A* **392**, 45 (1984).
- [3] F. D. M. Haldane, *Phys. Rev. Lett.* **61**, 2015 (1988).
- [4] F. D. M. Haldane and S. Raghu, *Phys. Rev. Lett.* **100**, 013904 (2008).
- [5] S. Raghu and F. D. M. Haldane, *Phys. Rev. A* **78**, 033834 (2008).
- [6] T. Ozawa and H. M. Price, *Nat. Rev. Phys.* **1**, 349 (2019).
- [7] K. S. Novoselov, A. K. Geim, S. V. Morozov, D. Jiang, M. I. Katsnelson, I. V. Grigorieva, S. V. Dubonos, and A. A. Firsov, *Nature (London)* **438**, 197 (2005).
- [8] S. M. Young, S. Zaheer, J. C. Y. Teo, C. L. Kane, E. J. Mele, and A. M. Rappe, *Phys. Rev. Lett.* **108**, 140405 (2012).
- [9] S. M. Young and C. L. Kane, *Phys. Rev. Lett.* **115**, 126803 (2015).
- [10] N. P. Armitage, E. J. Mele, and A. Vishwanath, *Rev. Mod. Phys.* **90**, 015001 (2018).
- [11] B. Yan and C. Felser, *Annu. Rev. Condens. Matter Phys.* **8**, 337 (2017).
- [12] B. Q. Lv, H. M. Weng, B. B. Fu, X. P. Wang, H. Miao, J. Ma, P. Richard, X. C. Huang, L. X. Zhao, G. F. Chen *et al.*, *Phys. Rev. X* **5**, 031013 (2015).
- [13] A. A. Soluyanov, D. Gresch, Z. Wang, Q. Wu, M. Troyer, X. Dai, and B. A. Bernevig, *Nature (London)* **527**, 495 (2015).
- [14] R.-P. Riwar, M. Houzet, J. S. Meyer, and Y. V. Nazarov, *Nat. Commun.* **7**, 11167 (2016).
- [15] I. Septembre, J. S. Meyer, D. D. Solnyshkov, and G. Malpuech, *Phys. Rev. B* **107**, 165301 (2023).
- [16] W. Voigt, *Philos. Mag. Ser. 4*, 90 (1902).
- [17] S. Richter, H.-G. Zirnstein, J. Zúñiga-Pérez, E. Krüger, C. Deparis, L. Trefflich, C. Sturm, B. Rosenow, M. Grundmann, and R. Schmidt-Grund, *Phys. Rev. Lett.* **123**, 227401 (2019).
- [18] Q. Liao, C. Leblanc, J. Ren, F. Li, Y. Li, D. Solnyshkov, G. Malpuech, J. Yao, and H. Fu, *Phys. Rev. Lett.* **127**, 107402 (2021).
- [19] M. Król, I. Septembre, P. Oliwa, M. Kędziora, K. Łempicka-Mirek, M. Muszyński, R. Mazur, P. Morawiak, W. Piecek, P. Kula *et al.*, *Nat. Commun.* **13**, 5340 (2022).
- [20] B. Mera and T. Ozawa, *Phys. Rev. B* **104**, 045104 (2021).
- [21] A. P. Schnyder, S. Ryu, A. Furusaki, and A. W. W. Ludwig, *Phys. Rev. B* **78**, 195125 (2008).
- [22] L. Fidkowski and A. Kitaev, *Phys. Rev. B* **81**, 134509 (2010).
- [23] C.-K. Chiu, J. C. Y. Teo, A. P. Schnyder, and S. Ryu, *Rev. Mod. Phys.* **88**, 035005 (2016).
- [24] J. Kruthoff, J. de Boer, J. van Wezel, C. L. Kane, and R.-J. Slager, *Phys. Rev. X* **7**, 041069 (2017).
- [25] Z. Wang, Y. D. Chong, J. D. Joannopoulos, and M. Soljačić, *Phys. Rev. Lett.* **100**, 013905 (2008).
- [26] Z. Wang, Y. Chong, J. D. Joannopoulos, and M. Soljačić, *Nature (London)* **461**, 772 (2009).
- [27] A. Kavokin, G. Malpuech, and M. Glazov, *Phys. Rev. Lett.* **95**, 136601 (2005).

- [28] A. V. Nalitov, D. D. Solnyshkov, and G. Malpuech, *Phys. Rev. Lett.* **114**, 116401 (2015).
- [29] S. Klembt, T. Harder, O. Egorov, K. Winkler, R. Ge, M. Bandres, M. Emmerling, L. Worschech, T. Liew, M. Segev *et al.*, *Nature (London)* **562**, 552 (2018).
- [30] C. L. Kane and E. J. Mele, *Phys. Rev. Lett.* **95**, 146802 (2005).
- [31] M. Z. Hasan and C. L. Kane, *Rev. Mod. Phys.* **82**, 3045 (2010).
- [32] D. Xiao, W. Yao, and Q. Niu, *Phys. Rev. Lett.* **99**, 236809 (2007).
- [33] M. Hafezi, E. A. Demler, M. D. Lukin, and J. M. Taylor, *Nat. Phys.* **7**, 907 (2011).
- [34] A. B. Khanikaev, S. Hossein Mousavi, W.-K. Tse, M. Kargarian, A. H. MacDonald, and G. Shvets, *Nat. Mater.* **12**, 233 (2013).
- [35] L.-H. Wu and X. Hu, *Phys. Rev. Lett.* **114**, 223901 (2015).
- [36] S. Barik, H. Miyake, W. DeGottardi, E. Waks, and M. Hafezi, *New J. Phys.* **18**, 113013 (2016).
- [37] S. Barik, A. Karasahin, C. Flower, T. Cai, H. Miyake, W. DeGottardi, M. Hafezi, and E. Waks, *Science* **359**, 666 (2018).
- [38] G. Lévêque, Y. Pennec, P. Szriftgiser, A. Amo, and A. Martínez, [arXiv:2301.10565](https://arxiv.org/abs/2301.10565).
- [39] Y. Zhou, N. Zhang, D. J. Bisharat, R. J. Davis, Z. Zhang, J. Friend, P. R. Bandaru, and D. F. Sievenpiper, *Phys. Rev. Appl.* **19**, 024053 (2023).
- [40] J.-K. Yang, Y. Hwang, and S. S. Oh, *Phys. Rev. Res.* **3**, L022025 (2021).
- [41] R. J. Davis, Y. Zhou, D. J. Bisharat, P. R. Bandaru, and D. F. Sievenpiper, *Phys. Rev. B* **106**, 165403 (2022).
- [42] D. D. Solnyshkov, A. V. Nalitov, and G. Malpuech, *Phys. Rev. Lett.* **116**, 046402 (2016).
- [43] A. Imamoglu, R. J. Ram. S. Pau, and Y. Yamamoto, *Phys. Rev. A* **53**, 4250 (1996).
- [44] A. Kavokin, J. J. Baumberg, G. Malpuech, and F. P. Laussy, *Microcavities* (Oxford University Press, Oxford, UK, 2017).
- [45] L. Pilozzi and C. Conti, *Phys. Rev. B* **93**, 195317 (2016).
- [46] P. St-Jean, V. Goblot, E. Galopin, A. Lemaître, T. Ozawa, L. Le Gratiet, I. Sagnes, J. Bloch, and A. Amo, *Nat. Photonics* **11**, 651 (2017).
- [47] M. Dusel, S. Betzold, T. H. Harder, M. Emmerling, J. Beierlein, J. Ohmer, U. Fischer, R. Thomale, C. Schneider, S. Hofling *et al.*, *Nano Lett.* **21**, 6398 (2021).
- [48] T. H. Harder, M. Sun, O. A. Egorov, I. Vakulchyk, J. Beierlein, P. Gagel, M. Emmerling, C. Schneider, U. Peschel, I. G. Savenko *et al.*, *ACS Photonics* **8**, 1377 (2021).
- [49] G. Harari, M. A. Bandres, Y. Lumer, Y. Plotnik, D. N. Christodoulides, and M. Segev, in *2016 Conference on Lasers and Electro-Optics (CLEO), San Jose, CA* (Optica Publishing Group, San Jose, California, 2016), p. FM3A.3.
- [50] B. Bahari, A. Ndao, F. Vallini, A. El Amili, Y. Fainman, and B. Kanté, *Science* **358**, 636 (2017).
- [51] M. A. Bandres, S. Wittek, G. Harari, M. Parto, J. Ren, M. Segev, D. N. Christodoulides, and M. Khajavikhan, *Science* **359**, eaar4005 (2018).
- [52] Y. Zeng, U. Chattopadhyay, B. Zhu, B. Qiang, J. Li, Y. Jin, L. Li, A. G. Davies, E. H. Linfield, B. Zhang *et al.*, *Nature (London)* **578**, 246 (2020).
- [53] J.-H. Choi, W. E. Hayenga, Y. G. Liu, M. Parto, B. Bahari, D. N. Christodoulides, and M. Khajavikhan, *Nat. Commun.* **12**, 3434 (2021).
- [54] Y. V. Kartashov and D. V. Skryabin, *Phys. Rev. Lett.* **122**, 083902 (2019).
- [55] M. Li, I. Sinev, F. Benimetskiy, T. Ivanova, E. Khestanova, S. Kiriushechkina, A. Vakulenko, S. Guddala, M. Skolnick, V. M. Menon *et al.*, *Nat. Commun.* **12**, 4425 (2021).
- [56] M. Zamfirescu, A. Kavokin, B. Gil, G. Malpuech, and M. Kaliteevski, *Phys. Rev. B* **65**, 161205(R) (2002).
- [57] G. Malpuech, A. Kavokin, A. Di Carlo, J. Baumberg, F. Compagnone, P. Lugli, and M. Zamfirescu, *Phys. Status Solidi A* **190**, 181 (2002).
- [58] S. Christopoulos, G. Baldassarri Höger von Högersthal, A. J. D. Grundy, P. G. Lagoudakis, A. V. Kavokin, J. J. Baumberg, G. Christmann, R. Butté, E. Feltin, J.-F. Carlin, and N. Grandjean, *Phys. Rev. Lett.* **98**, 126405 (2007).
- [59] F. Li, L. Orosz, O. Kamoun, S. Bouchoule, C. Brimont, P. Disseix, T. Guillet, X. Lafosse, M. Leroux, J. Leymarie *et al.*, *Phys. Rev. Lett.* **110**, 196406 (2013).
- [60] O. Jamadi, F. Reveret, P. Disseix, F. Medard, J. Leymarie, A. Moreau, D. Solnyshkov, C. Deparis, M. Leroux, E. Cambril *et al.*, *Light Sci. Appl.* **7**, 82 (2018).
- [61] H. Souissi, M. Gromovyi, T. Gueye, C. Brimont, L. Doyennette, D. D. Solnyshkov, G. Malpuech, E. Cambril, S. Bouchoule, B. Alloing, S. Rennesson, F. Semon, J. Zuniga-Perez, and T. Guillet, *Phys. Rev. Appl.* **18**, 044029 (2022).
- [62] A. Delphan, M. N. Makhonin, T. Isoniemi, P. M. Walker, M. S. Skolnick, D. N. Krizhanovskii, D. V. Skryabin, J.-F. Carlin, N. Grandjean, and R. Butté, *APL Photonics* **8**, 021302 (2023).
- [63] F. Wen, S. David, X. Checoury, M. El Kurdi, and P. Boucaud, *Opt. Express* **16**, 12278 (2008).
- [64] W. Noh, H. Nasari, H.-M. Kim, Q. Le-Van, Z. Jia, C.-H. Huang, and B. Kanté, *Opt. Lett.* **45**, 4108 (2020).
- [65] H. C. Po, *J. Phys.: Condens. Matter* **32**, 263001 (2020).
- [66] J. Luo, Z. Du, Y. Guo, C. Liu, W. Zhang, and X. Guo, *Nanophotonics* **10**, 4523 (2021).
- [67] E. Wen, D. J. Bisharat, R. J. Davis, X. Yang, and D. F. Sievenpiper, *Phys. Rev. Appl.* **17**, 064008 (2022).
- [68] O. Herrfurth, S. Richter, M. Rebarz, S. Espinoza, J. Zúñiga-Pérez, C. Deparis, J. Leveillee, A. Schleife, M. Grundmann, J. Andreasson *et al.*, *Phys. Rev. Res.* **3**, 013246 (2021).
- [69] See Supplemental Material at <http://link.aps.org/supplemental/10.1103/PhysRevB.107.155304> for the refractive index of the TiO<sub>2</sub> used in the simulations.
- [70] J. Hopfield, *Phys. Rev.* **112**, 1555 (1958).
- [71] C. Teng, J. Muth, Ü. Özgür, M. Bergmann, H. Everitt, A. Sharma, C. Jin, and J. Narayan, *Appl. Phys. Lett.* **76**, 979 (2000).
- [72] Close to the exciton resonance, the refractive index of ZnO varies rapidly with the energy and acquires large values, so the spatial mesh has to be extremely fine. Moreover, the structure containing an interface is approximately 20 times larger than a unit cell, which explains that the simulation time needed is larger for a structure with an interface than without.
- [73] A. Kavokin and G. Malpuech, *Cavity Polaritons* (Elsevier, Amsterdam, 2003).

- [74] H. Haug and S. W. Koch, *Quantum Theory of the Optical and Electronic Properties of Semiconductors* (World Scientific, Singapore, 2009).
- [75] J.-R. Chen, T.-C. Lu, Y.-C. Wu, S.-C. Lin, W.-R. Liu, W.-F. Hsieh, C.-C. Kuo, and C.-C. Lee, *Appl. Phys. Lett.* **94**, 061103 (2009).
- [76] M. Mihailovic, A.-L. Henneghien, S. Faure, P. Disseix, J. Leymarie, A. Vasson, D. Buell, F. Semond, C. Morhain, and J. Z. Pérez, *Opt. Mater. (Amsterdam)* **31**, 532 (2009).
- [77] A. Trichet, L. Sun, G. Pavlovic, N. A. Gippius, G. Malpuech, W. Xie, Z. Chen, M. Richard, and L. S. Dang, *Phys. Rev. B* **83**, 041302(R) (2011).
- [78] J. Ciers, D. D. Solnyshkov, G. Callsen, Y. Kuang, J.-F. Carlin, G. Malpuech, R. Butté, and N. Grandjean, *Phys. Rev. B* **102**, 155304 (2020).
- [79] Y. Gong, S. Wong, A. J. Bennett, D. L. Huffaker, and S. S. Oh, *ACS Photonics* **7**, 2089 (2020).